Publ. Astron. Soc. Japan (2022) 74 (4), 904–922
https://doi.org/10.1093/pasj/psac044
Advance Access Publication Date: 2022 June 30

A super-Earth orbiting near the inner edge of the habitable zone around the M4.5 dwarf Ross 508

Hiroki Harakawa [1,*] Takuya Takarada [2,3] Yui Kasagi [4] Teruyuki Hirano [2,3,4] Takayuki Kotani [2,3,4] Masayuki Kuzuhara [2,3] Masashi Omiya [2,3] Hajime Kawahara [5] Akihiko Fukui [6] Yasunori Hori [2,3] Hiroyuki Tako Ishikawa [2,3] Masahiro Ogihara [3,7,8] John Livingston [2,3,9] Timothy D. Brandt [10] Thayne Currie [1,11,12] Wako Aoki [3] Charles A. Beichman [13,14] Thomas Henning [15] Klaus Hodapp [16] Masato Ishizuka [9] Hideyuki Izumiura [17] Shane Jacobson [16] Markus Janson [18] Eiji Kambe [1] Takanori Kodama [6] Eiichiro Kokubo [3] Mihoko Konishi [19] Vigneshwaran Krishnamurthy [2,3] Tomoyuki Kudo [1] Takashi Kurokawa [2,20] Nobuhiko Kusakabe [2,3] Jungmi Kwon [9] Yuji Matsumoto [3] Michael W. McElwain [21] Koyu Mitsui [9] Takao Nakagawa [22] Norio Narita [2,6,23] Jun Nishikawa [3,4] Stevanus K. Nugroho [2,3] Eugene Serabyn [24] Takuma Serizawa [3,20] Aoi Takahashi [2,3] Akitoshi Ueda [2,3,4] Taichi Uyama [3,13,14] Sébastien Vievard [1,2] Ji Wang [25] John Wisniewski [26] Motohide Tamura [2,3,9] and Bun'ei Sato [27]

[1]Subaru Telescope, 650 North A'ohoku Place, Hilo, HI 96720, USA
[2]Astrobiology Center, 2-21-1 Osawa, Mitaka, Tokyo 181-8588, Japan
[3]National Astronomical Observatory of Japan, 2-21-1 Osawa, Mitaka, Tokyo 181-8588, Japan
[4]Department of Astronomical Science, The Graduate University for Advanced Studies, SOKENDAI, 2-21-1 Osawa, Mitaka, Tokyo 181-8588, Japan
[5]Department of Earth and Planetary Sciences, Graduate School of Science, The University of Tokyo, 7-3-1 Hongo, Bunkyo-ku, Tokyo 113-0033, Japan
[6]Komaba Institute for Science, The University of Tokyo, 3-8-1 Komaba, Meguro, Tokyo 153-8902, Japan
[7]Tsung-Dao Lee Institute, Shanghai Jiao Tong University, 520 Shengrong Road, Shanghai 201210, China
[8]Earth-Life Science Institute, Tokyo Institute of Technology, 2-12-1 Ookayama, Meguro, Tokyo 152-8550, Japan
[9]Department of Astronomy, Graduate School of Science, The University of Tokyo, 7-3-1 Hongo, Bunkyo-ku, Tokyo 113-0033, Japan
[10]Department of Physics, University of California, Santa Barbara, Santa Barbara, CA 93106, USA
[11]NASA-Ames Research Center, Moffett Field, CA 94035, USA
[12]Eureka Scientific, Oakland, 10 CA, USA
[13]Infrared Processing and Analysis Center, California Institute of Technology, 1200 E. California Boulevard, Pasadena, CA 91125, USA
[14]NASA Exoplanet Science Institute, Pasadena, CA 91125, USA
[15]Max-Planck-Institut für Astronomie, Königstuhl 17, 69117 Heidelberg, Germany
[16]University of Hawaii, Institute for Astronomy, 640 N. A'ohoku Place, Hilo, HI 96720, USA

[17]Okayama Branch, Subaru Telescope, National Astronomical Observatory of Japan, National Institute of Natural Sciences, Kamogata, Asakuchi, Okayama 719-0232, Japan
[18]Department of Astronomy, Stockholm University, SE-10691, Stockholm, Sweden
[19]Faculty of Science and Technology, Oita University, 700 Dannoharu, Oita, Oita 870-1192, Japan
[20]Institute of Engineering, Tokyo University of Agriculture and Technology, 2-24-16 Nakacho, Koganei, Tokyo 184-8588, Japan
[21]Exoplanets and Stellar Astrophysics Laboratory, NASA Goddard Space Flight Center, Greenbelt, MD 20771, USA
[22]Institute of Space and Astronautical Science, Japan Aerospace Exploration Agency, 3-1-1 Yoshinodai, Chuo-ku, Sagamihara, Kanagawa 252-5210, Japan
[23]Instituto de Astrofísica de Canarias (IAC), 38205 La Laguna, Tenerife, Spain
[24]Jet Propulsion Laboratory, California Institute of Technology, Pasadena, CA 91109, USA
[25]Department of Astronomy, The Ohio State University, 100 W 18th Ave, Columbus, OH 43210, USA
[26]Department of Physics and Astronomy, University of Oklahoma, 440 West Brooks Street, Norman, OK 73019, USA
[27]Department of Earth and Planetary Sciences, Tokyo Institute of Technology, 2-12-1 Ookayama, Meguro-ku, Tokyo 152-8551, Japan

*E-mail: harakawa@naoj.org

Received 2022 March 6; Accepted 2022 May 23

Abstract

We report the near-infrared radial velocity (RV) discovery of a super-Earth planet on a 10.77 d orbit around the M4.5 dwarf Ross 508 ($J_{\rm mag} = 9.1$). Using precision RVs from the Subaru Telescope IRD (InfraRed Doppler) instrument, we derive a semi-amplitude of $3.92^{+0.60}_{-0.58}$ m s^{-1}, corresponding to a planet with a minimum mass $m\sin i = 4.00^{+0.53}_{-0.55}\ M_{\oplus}$. We find no evidence of significant signals at the detected period in spectroscopic stellar activity indicators or MEarth photometry. The planet, Ross 508 b, has a semi-major axis of $0.05366^{+0.00056}_{-0.00049}$ au. This gives an orbit-averaged insolation of $\approx$1.4 times the Earth's value, placing Ross 508 b near the inner edge of its star's habitable zone. We have explored the possibility that the planet has a high eccentricity and its host is accompanied by an additional unconfirmed companion on a wide orbit. Our discovery demonstrates that the near-infrared RV search can play a crucial role in finding a low-mass planet around cool M dwarfs like Ross 508.

Key words: infrared: planetary systems — planets and satellites: terrestrial planets — techniques: radial velocities

1 Introduction

Since the discovery of 51 Pegasi b around a solar-type star (Mayor & Queloz 1995), precision radial velocity (RV) searches have discovered nearly a thousand exoplanets (Schneider et al. 2011). More recently, transit surveys, with observatories including CoRoT (Baglin et al. 2006), Kepler (Borucki et al. 2010), and the Transiting Exoplanet Survey Satellite (TESS; Ricker et al. 2015) have discovered several thousand more. Exoplanets are known to orbit various types of stars such as solar-type stars (e.g., Lissauer et al. 2011), low-mass M dwarfs (Gillon et al. 2017), evolved stars (Teng et al. 2022), and stellar remnants (e.g., Vanderburg et al. 2020). Among them, M-type stars are especially promising targets for the detection of Earth-like planets. These stars' small sizes make transits relatively deep, and their low luminosities make the habitable zone close to the star where the RV amplitude is larger.

Nevertheless, exoplanet discoveries around cool M dwarfs are still limited.[1] Most exoplanet surveys have used optical CCDs in their cameras but such cool stars emit

[1] Only three (two) stars with effective temperatures less than 3000 K have been discovered to host planets via the RV (transit) technique, according to a query of the NASA Exoplanet Archive in 2022 February. Note that the effective temperatures from the TESS Input Catalog (TIC; Stassun et al. 2019) were adopted for the majority of the sample.

most of their energy in the near-infrared (NIR). One of the most effective ways to search for planets around cool M-type stars is to use an infrared-sensitive high-dispersion and high-precision spectrograph. Recently, several teams have commissioned NIR spectrographs for high-precision RV surveys, including CARMENES (Calar Alto high-Resolution search for M dwarfs with Exoearths with Near-infrared and optical Echelle Spectrographs; Quirrenbach et al. 2016), HPF (Habitable Planet Finder; Mahadevan et al. 2014), and SPIROU (SPectropolarimetre InfraROUge; Thibault et al. 2012). The RV surveys performed with those spectrographs have so far reported a few detections of planetary systems around M dwarfs cooler than ∼3000 K (e.g., Zechmeister et al. 2019), while they have reported dozens of exoplanets around stars with effective temperature higher than ∼3000 K. It is notable that optical RV measurements have been primarily used for those detections; for example, the terrestrial planets around Teegarden's star were discovered using the optical channel of CARMENES (Zechmeister et al. 2019). High-precision RV measurements in the NIR facilitate the detection of planets around cooler M dwarfs, which remains a frontier in exoplanet exploration.

The IRD (InfraRed Doppler instrument) is a high-precision, high-dispersion ($R = 70000$) NIR spectrograph mounted on the Subaru 8.2 m telescope (Tamura et al. 2012; Kotani et al. 2018). To achieve a velocity precision of 2–3 m s^{-1}, IRD is aided by a wide-band laser-frequency comb (LFC: Kashiwagi et al. 2016; Kokubo et al. 2016), and an adaptive optics, enabling the use of a narrow slit-width. The combination of a large-aperture telescope with high RV precision in the NIR thus makes IRD one of the best instruments for studying cool stars, in particular late M dwarfs, the flux peaks of which are located in the NIR. In 2019 February, we started an extensive RV survey program for nearby mid-to-late M-type dwarfs within the Subaru Strategic Program (SSP) framework.[2] This program employs IRD with the aim of detecting planets down to Earth-mass in the habitable zones (HZs) of nearby late M dwarfs. The capabilities of IRD allow the systematic survey of fainter, and thus later-type, M dwarfs than ever before.

In this paper, we present the first exoplanet discovery from the IRD-SSP campaign, a super-Earth that orbits near the inner edge of the HZ around Ross 508 (the star is also known as LSPM J1523+1727), which is an M4.5-type dwarf (Koizumi et al. 2021) at a distance of 11.2 pc (Gaia Collaboration 2021) from Earth. In section 2, we describe the observations and data reduction of Ross 508. In section 3 we present our analysis of the fundamental properties and activity of Ross 508, along with the determination of the planet's orbit from the RV measurements. Finally, in section 4, we discuss the uniqueness of the planet and its potential formation processes, concluding with a summary.

[2] See "Search for Planets like Earth around Late-M Dwarfs: Precise Radial Velocity Survey with IRD (PI: B. Sato)," 2018, Subaru Strategic Program proposal ⟨https://www.naoj.org/Science/SACM/Senryaku/IRD_180520235849.pdf⟩.

2 Observations

2.1 Target selection

Ross 508 was observed as part of the IRD-SSP survey because of its low mass ($M < 0.25\,M_{\odot}$), low temperature ($T_{\rm eff} < 3400$ K), low $v\sin i$ (<5 km s^{-1}), and low stellar activity. The initial target list was prepared based on literature measurements satisfying the above criteria supplemented with optical medium-resolution spectroscopic observations (Koizumi et al. 2021).[2] Stars with no rotation period and $v\sin i$ measurements were required to have non-detections of Hα emission, which is expected for inactive and slowly rotating stars. We continually refine our target list, dropping stars from our long-term monitoring campaign if IRD spectra show them to be double-lined spectroscopic binaries or rapid rotators, or if we detect large RV variations suggestive of stellar companions. With these screening data, we plan to select about 60 mid and late M dwarfs with low RV variability and high RV precision for the RV monitors, after about three-year observations of its planned five-year survey period.

2.2 Observations and data reduction

We obtained 102 high-resolution, high-S/N spectra of Ross 508 using IRD over ≈ three years from 2019 to 2021. All stellar spectra were obtained simultaneously with LFC spectra to provide a fiducial wavelength reference for precision RV measurements. The typical exposure time for each frame was 600 s, achieving an S/N ratio of about 90 per pixel at 1 μm wavelength.

The two H2RG (HAWAII-2RG) detectors installed in IRD show mutually independent bias levels for each readout channel. We thus used our bias subtraction code optimized for those two detectors to suppress bias counts (Kuzuhara et al. 2018). We also subtracted correlated read noise by applying a commonly used technique for H2RG detectors (e.g., Brandt et al. 2013) to the science pixels in our images with the temporal masks to the 2D-spectra.

Following the removal of bias and read noise, we used `IRAF` (`echelle` package) for subsequent échelle data reduction procedures, such as scattered light subtraction, flat fielding, and extraction of one-dimensional spectra. Preliminary wavelength calibrations were done using Th-Ar spectra, but we obtained precise RV measurements using LFC spectra (see Hirano et al. 2020, for details). Details of the RV measurements from the 1D spectra are described in sub-subsection 3.3.1.

Table 1. Stellar parameters of Ross 508.

Parameter	Value	Reference
α (J2000.0)	$15^{\rm h}23^{\rm m}50\overset{\rm s}{.}699$	Gaia eDR3
δ (J2000.0)	$+17°27'37\overset{''}{.}30$	Gaia eDR3
ϖ (mas)	89.1284 ± 0.0331	Gaia eDR3
Distance (pc)	11.2183 ± 0.0035	Bailer-Jones et al. (2021)
RUWE	1.487	Gaia eDR3
G (mag)	12.1952 ± 0.0029	Gaia eDR3
$G_{\rm BP}$ (mag)	13.9882 ± 0.0044	Gaia eDR3
$G_{\rm RP}$ (mag)	10.9204 ± 0.0042	Gaia eDR3
J (mag)	9.105 ± 0.024	2MASS
$K_{\rm s}$ (mag)	8.279 ± 0.023	2MASS
Spectral type	M4.5	Koizumi et al. (2021)
$T_{\rm eff}$ (K)	3071^{+34}_{-22}	This work
$\log g$ (cgs)	5.039 ± 0.027	This work
$L_\star$ ($L_\odot$)	$3.589^{+0.067}_{-0.071} \times 10^{-3}$	This work
$M_\star$ ($M_\odot$)	0.1774 ± 0.0045	This work
$R_\star$ ($R_\odot$)	0.2113 ± 0.0063	This work
$\rho_\star$ (g cm^{-3})	$26.5^{+2.5}_{-2.3}$	This work
[Fe/H] (dex)	-0.20 ± 0.20	Ishikawa et al. (2022)

3 Analysis and results

3.1 Stellar parameters

We derive the fundamental stellar parameters for Ross 508 using a combination of literature measurements and IRD spectra. Table 1 summarizes all of our adopted stellar parameters including the ones we derive below.

For Ross 508's metallicity, we adopt its iron abundance [Fe/H] determined by Ishikawa et al. (2022) from the same IRD spectra that we use here. They conducted the equivalent width analysis on the atomic absorption lines of Na, Mg, Ca, Ti, Cr, Mn, Fe, and Sr to derive individual elemental abundances that are consistent with each other. The abundance of individual elements will help to constrain the detailed geophysical properties of the planets, although it is beyond the scope of this paper. Ross 508 is a relatively metal-poor star, but the abundance ratio of each of its elements is consistent with the solar composition within the errors. Their abundance and kinematic analyses show characteristics between the thin and thick galactic disks, suggesting the possibility of a relatively old population.

We next analyzed the spectral energy distribution (SED) of Ross 508 to estimate its effective temperature and luminosity. The SED was calculated from the magnitudes in the G, B_P, and R_P bands from Gaia EDR3 (Gaia Collaboration 2021), J, H, and $K_{\rm s}$ bands from 2MASS (Skrutskie et al. 2006), and *W1*, *W2*, *W3*, and *W4* bands from WISE (Cutri et al. 2021). We fit BT-Settl synthetic spectrum models (Allard 2014) to the SED using the following parameters: effective temperature $T_{\rm eff}$, log surface gravity $\log g$, and $\log(R_{\rm s}/D)$, where $R_{\rm s}$ and D are the radius and distance of the star, respectively. We assumed no interstellar extinction. We calculated the posterior probability distributions of these parameters using the Markov Chain Monte Carlo (MCMC) method implemented in the Python package `emcee` (Foreman-Mackey et al. 2013). In each MCMC step, a synthetic spectrum was calculated by linearly interpolating the model grid for a given set of parameters, where the metallicity value was randomly chosen from a normal distribution of $\mathcal{N}(-0.20, 0.20)$ dex. A white noise jitter term, $\sigma_{\rm jitter}$, was also fitted for each of the Gaia EDR3, 2MASS, and WISE data sets such that the magnitude uncertainty was given by $\sqrt{\sigma_{\rm cat}^2 + \sigma_{\rm jitter}^2}$, where $\sigma_{\rm cat}$ is the catalogued uncertainty in magnitude. From the posteriors, we derived $T_{\rm eff} = 3071^{+34}_{-22}$ K, $\log g = 5.26^{+0.18}_{-0.35}$ (cgs), and $\log(R_{\rm s}/D) = -9.3721^{+0.0062}_{-0.0085}$ (cgs). Adopting $D = 11.2183 \pm 0.0035$ pc from Bailer-Jones et al. (2021) which is estimated based on the GaiaEDR3 parallax, we obtained $R_{\rm s} = 0.2111^{+0.0030}_{-0.0041}\ R_\odot$, which also yielded the stellar luminosity of $L_{\rm s} = 3.584^{+0.067}_{-0.071} \times 10^{-3}\ L_\odot$ via the Stefan–Boltzmann law. Note that the median values of the white noise jitter terms are 0.089, 0.074, and 0.00050 mag for the Gaia EDR3, 2MASS, and WISE data sets, respectively. The relatively large jitter values in the Gaia EDR3 and 2MASS data sets might reflect the challenges for the stellar models for cool stars.

Based on the stellar metallicity reported in Ishikawa et al. (2022), the effective temperature derived above, and the parameters in the literature (i.e., the Gaia parallax and 2MASS magnitudes), we inferred the physical parameters of Ross 508, including the stellar mass, which is required to estimate the planet mass. We made use of the empirical formulae by Mann et al. (2015, 2019) for the stellar radius and mass, for which the apparent $K_{\rm s}$-band magnitude of $m_{K_{\rm s}} = 8.279 \pm 0.023$ mag was adopted from the 2MASS catalog. We implemented a Monte Carlo simulation to estimate the uncertainties of the output parameters, accounting for the statistical error of the input parameters as well as the systematic error of the empirical formulae. We obtained a stellar radius and mass of $0.2113 \pm 0.0063\ R_\odot$ and $0.1774 \pm 0.0045\ M_\odot$, respectively, which yield a mean stellar density of $26.5^{+2.5}_{-2.2}$ g cm^{-3} and a surface gravity of $\log g = 5.038 \pm 0.027$ (cgs). This surface gravity is consistent with that derived from BT-Settl model atmospheres.

3.2 Adaptive optics imaging

Ross 508 has a relatively high renormalized unit weight error (RUWE) of 1.48 in Gaia EDR3, implying that this star might be associated with an unseen companion. In order to search for a possible companion, we analyzed adaptive optics high-resolution images of Ross 508 obtained with the Fiber Injection Monitor (FIM) camera of IRD. FIM is an

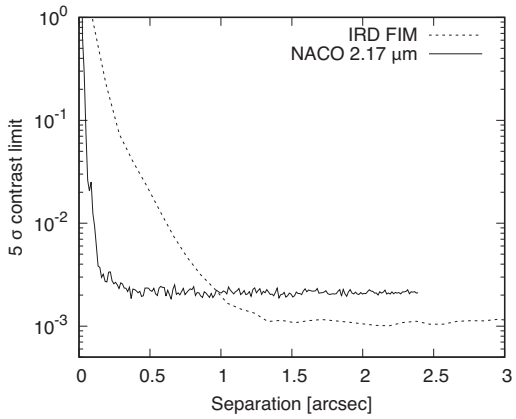

Fig. 1. 5σ contrast limits around Ross 508. The solid line shows the contrast limit from VLT/NACO in the NB 2.17 filter. The dashed line shows the contrast limit from the IRD FIM camera, which has a sensitivity over wavelengths ranging from 0.83 to 1.05 μm.

AO-assisted CCD camera sensitive to wavelengths of 0.83 to 1.05 μm, and is used to monitor a target's position during observations. The CCD camera is usually used to feed the light into the IRD fiber. The FIM observations were performed every time, just before RV measurements of IRD, but we selected images taken only under good seeing conditions. The final selected images consist of 33 frames with a total integration time of 74 seconds. The FWHM of the final combined point spread function (PSF) is 0.″19, and the 5σ raw contrast limit is shown in figure 1. We also processed archival the Very Large Telescope with the Nasmyth Adaptive Optics System and Near-Infrared Imager and Spectrograph (VLT/NACO) data for Ross 508 [program ID: 71.C-0388(A), PI: J.-L. Beuzit] obtained with a narrow-band filter at 2.17 μm (NB 2.17 filter, 2.166 $\pm$ 0.023 μm) using a well-tested general-use pipeline (Currie et al. 2011). A total of 44 frames with an integration time of 2 s each were reduced and combined to create the final high-quality image. No speckle subtraction techniques were applied to either the FIM or NACO images. We found no stellar companions at a separation wider than $\sim$0.″1 from the central star. At separations exterior to 0.″25 ($r_{\rm proj} \sim 2.8$ au), the comparison of the contrast limits with the Baraffe et al. (2003) evolutionary models enables us to rule out companions that are more massive than 35 $M_{\rm J}$ or 70 $M_{\rm J}$ for an assumed system age of 1 Gyr or 10 Gyr, respectively.

3.3 Radial velocity and orbital solutions

3.3.1 Radial velocity measurements

For each wavelength-calibrated spectrum, we measured precise RVs following the standard RV-analysis pipeline for IRD (Hirano et al. 2020); we refer to that paper for a detailed discussion. In short, the pipeline extracts the instantaneous instrumental profile (IP) of the spectrograph from the simultaneously injected LFC spectrum, and generates an IP-deconvolved, telluric-free template spectrum for the target star using multiple IRD spectra. Using this template, individual spectral segments for each IRD spectrum are fitted by the forward modeling technique, in which telluric absorption features are simultaneously optimized. The resulting relative RV values as well as their uncertainties are summarized in table 2. The RV internal error was typically 2–3 m s^{-1} for each frame.

We corrected for RV drifts that are attributed to the Earth's rotation and orbital motion (i.e., barycentric RV correction) using the TEMPO2 software (Edwards et al. 2006). TEMPO2 also corrects for perspective acceleration, which is $\approx$0.45 m s^{-1} yr^{-1} for Ross 508. IRD applies multiple readouts to its two H2RG detectors during an exposure (Kuzuhara et al. 2018). Accordingly, we computed the telluric RV using the time when half of the total signal was counted, which was determined by monitoring the photon counts acquired by the detectors every $\sim$1.5 s.

We note that one of the causes of long-term RV measurement instability originates from the IRD instrument. We evaluated the instrumental error via both laboratory experiments and on-sky monitoring observations of an RV standard star, GJ 699. These two methods resulted in the same value of 2 m s^{-1}. From the laboratory experiments, we found that the main sources of instrumental error are the intra- and inter-pixel sensitivity variations of the detector (0.96 m s^{-1}), as well as the modal noise ($\sim$1.2 m s^{-1}) caused by PSF instability (Kotani et al. 2018). We found a total RV error of 3 m s^{-1} over 718 d of on-sky monitoring observations of GJ 699, which (assuming no planet around the star) yields an instrument-derived error of about 2 m s^{-1} (T. Kotani et al. in preparation). In the case of Ross 508, we assume that the RV measurements are affected by the same amount of instrumental noise. Note that table 2 provides RV uncertainties that do not include the instrument-derived errors.

3.3.2 Orbital solutions

We searched for periodicity in our RV time series before performing an orbital fit. We computed the Generalized Lomb–Scargle (GLS) periodogram (Zechmeister & Kürster 2009) for all RV data and for the window function, and identified three significant peaks at 10.7510, 0.9124, and 1.1023 d in order of decreasing GLS power (figure 2). Hereafter, all the false alarm probability (FAP) values were derived by analytical estimation reported in Baluev (2008). For the window function, we identified a single peak at 0.9972 d. In the GLS periodogram analysis, we set the RV error to be

Table 2. RVs for Ross 508.

BJD (−2450000)	RV ($m\,s^{-1}$)	Uncertainty ($m\,s^{-1}$)
8540.101484	−3.40	2.50
8565.084859	−2.30	2.43
8623.965979	−5.06	4.36
8623.971075	−7.11	2.71
8623.984402	0.27	3.14
8623.988127	−7.98	3.13
8656.804690	1.10	2.37
8736.724410	4.01	3.80
9004.939392	7.70	2.23
9004.946975	2.95	2.24
9005.972814	7.39	2.99
9005.980543	−1.40	2.69
9005.988855	3.97	2.84
9006.960442	−3.99	2.35
9006.967935	5.54	2.42
9007.882653	−2.05	2.30
9007.890162	2.98	2.30
9010.965542	−0.56	2.21
9010.973732	2.87	2.32
9011.918730	−0.84	2.22
9012.987404	−7.40	3.00
9012.993618	1.11	2.89
9014.952306	2.15	2.39
9014.959983	8.99	2.31
9017.952195	0.52	2.35
9017.959774	−3.71	2.43
9029.955337	4.42	2.25
9029.962978	0.18	2.22
9030.952815	−2.23	2.32
9030.960649	−0.90	2.30
9031.947822	−6.02	2.62
9031.955839	−2.77	2.44
9032.950886	−4.22	2.26
9032.958518	−8.38	2.30
9033.958650	−4.60	2.21
9033.966256	−2.75	2.13
9034.876530	−0.86	2.24
9034.884052	−0.05	2.18
9035.952939	2.06	2.39
9035.960628	0.34	2.31
9036.946364	6.51	2.33
9036.953908	7.24	2.31
9037.954089	4.63	2.53
9037.961776	0.57	2.47
9052.760439	1.09	2.58
9052.767841	−0.41	2.48
9054.740438	−6.13	2.58
9054.747908	−2.84	2.56
9055.737313	−1.26	2.79
9055.746024	−0.83	2.84
9062.738505	−7.60	2.64

Table 2. (Continued)

BJD (−2450000)	RV ($m\,s^{-1}$)	Uncertainty ($m\,s^{-1}$)
9062.746918	−1.06	2.63
9064.753007	−6.63	2.57
9065.730471	−3.30	2.60
9065.738626	1.92	2.60
9068.828720	7.37	3.48
9068.835744	4.97	3.17
9301.100420	−13.15	12.78
9301.924685	−4.96	3.52
9301.931132	−7.24	4.16
9305.012038	3.51	2.55
9305.021274	0.05	2.44
9321.988167	0.33	3.39
9321.991843	6.56	3.47
9329.979601	7.24	3.54
9329.984625	3.49	3.38
9335.998818	1.56	2.38
9336.006043	−0.96	2.38
9336.903887	1.66	2.31
9336.914754	1.94	2.26
9352.843703	0.65	2.73
9352.850681	1.97	2.70
9353.824596	−5.58	2.71
9353.829970	−4.19	2.77
9354.825976	−0.43	2.59
9354.832940	−2.78	2.60
9367.811663	1.07	2.90
9367.817009	−4.90	2.68
9368.804957	−2.86	2.76
9368.809560	0.26	2.74
9369.812588	2.78	2.80
9369.817475	1.25	2.81
9370.812156	1.10	2.47
9370.818195	7.52	2.55
9371.828379	8.15	2.36
9371.834659	2.45	2.42
9372.819000	2.06	2.48
9372.825454	−2.33	2.42
9410.740034	0.57	3.07
9410.743733	−4.85	3.02
9411.743618	−3.48	3.61
9411.747263	2.08	3.62
9452.777252	8.36	3.56
9452.780933	2.07	3.63
9453.799319	4.47	3.62
9453.803015	9.77	3.61
9455.725685	4.62	3.00
9455.731175	13.25	3.02
9468.728240	9.62	3.12
9468.733409	12.50	3.08
9486.714323	1.74	3.52
9486.719672	4.35	3.13

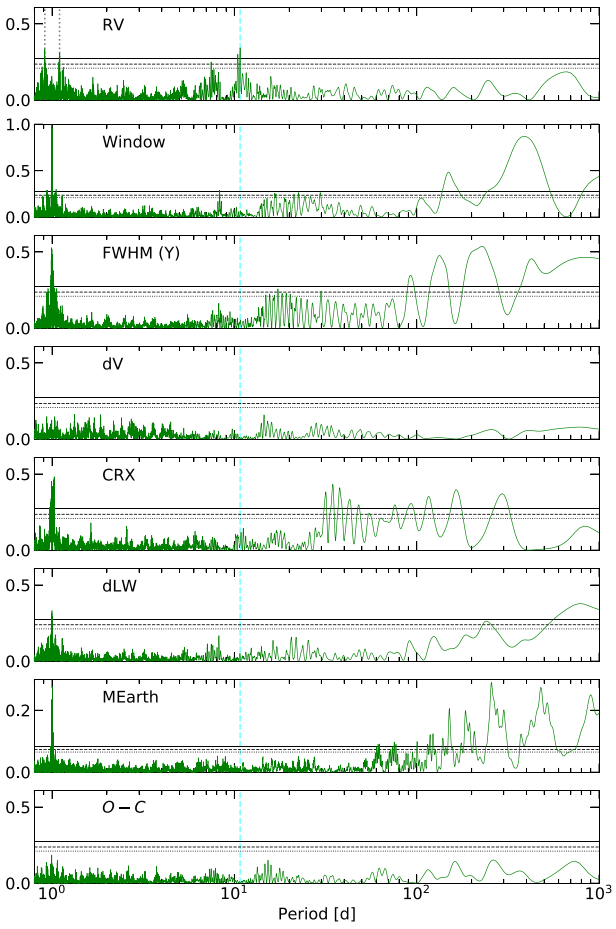

Fig. 2. From top to bottom: GLS periodograms of the RV time series, window function of the RV sampling, FWHM in the *Y*-band region, dV, CRX, dLW, MEarth photometry, and residual of the RV fitting. The dashed vertical line indicates the RV period at 10.7510 d, while the vertical gray dotted lines show the estimated aliases. See the main text for details of those values. The FAP values corresponding to 0.1%, 1%, and 5% are shown with solid, dashed, and dotted horizontal lines, respectively.

$\sqrt{\sigma_i^2 + \sigma_{\rm inst}^2}$, where σ_i is the RV uncertainty of an ith observation and $\sigma_{\rm inst}$ is the instrument-derived error described in sub-subsection 3.3.1.

Although the RV periodogram shows several significant periodicities, we first investigate whether some of these represent cases of aliasing, which generally appears in periodograms of discretely sampled time-series data. To distinguish aliases from physical signals, we performed a simple alias analysis based on the computed periodograms. In general, when sampling a sine wave of frequency f at sampling frequency $f_{\rm s}$, the sample is indistinguishable from any other sample of the sine curve whose frequency is $f_{\rm signal}(N) = |f - Nf_{\rm s}|$ (where $N = 0, \pm1, \pm2, \cdots$, and $f_{\rm signal}(0) = f$ is the actual signal frequency) as they yield identical sets of data. Those frequencies other than $N = 0$ are aliases that should be addressed. This equation assumes $f_{\rm s}$ as a perfectly evenly spaced sampling, and of course, the actual observations will not be carried out with such an ideal interval. However, since the window function of our data sampling shows a dominant power on almost a single frequency, we should be able to estimate the approximate effect of aliasing by applying this equation. We here assumed the most significant RV frequency of $1/10.7510\,{\rm d}^{-1}$ to be a physical one and the sampling frequency to be the most significant window function peak of $1/0.9972\,{\rm d}^{-1}$. If $N = +1$ and $N = -1$, this yields $1/1.0992\,{\rm d}^{-1}$ and $1/0.9125\,{\rm d}^{-1}$, respectively. These two frequencies are almost identical to those of the second and third significant peaks of the periodogram, showing that those two peaks in the periodogram can be interpreted as alias phenomena associated with a period of 10.751 d and its dominant sampling interval of 0.9972 d. We note that if we assumed the secondary peak of the window function at 390.25 d as a sampling frequency, the aliases were 11.05 and 10.46 d in the case of $N = +1$ and $N = -1$, respectively. The 10.46 d alias is almost identical to a peak of 10.45 d in the periodogram though its frequency is far beyond the Nyquist frequency of $0.5f_{\rm s} = 1/780.5$.

With a single significant periodicity at 10.75 d, we next performed a Keplerian fit to the RVs. As discussed in subsection 3.4, we found no significant activity signals at this period. We used `emcee` to explore the parameter spaces via MCMC. The initial states were randomly generated from the prior distributions shown in table 3. We ran the sampler until it satisfied the following convergence criterion: if the number of steps is greater than 100 times the autocorrelation length of each parameter, which is estimated every 1000 steps, and this estimate varies by less than 1%, then we assume that the chain has converged. The maximum steps was set to 30 million. The first 20% of the steps were discarded as burn-in, yielding a total of 24.0 million samples of the posterior distribution from the remaining steps.

Based on Gregory (2005), the likelihood function $\mathcal{L}$ used in this analysis is

$$\ln \mathcal{L} = -\frac{1}{2}\sum_i \left[\frac{(v_{i,\rm obs} - v_{i,\rm model})^2}{\sigma_i^2 + \sigma_{\rm jitt}^2} + \ln\left(\sigma_i^2 + \sigma_{\rm jitt}^2\right) \right], \quad (1)$$

where $v_{i,\rm obs}$ is the ith observed RV, $v_{i,\rm model}$ is the ith RV model calculated from the companion's Keplerian orbital motion, and $\sigma_{\rm jitt}$ is a jitter parameter to account for RV variations due to stellar activity and changes in instrumental stability. Priors of the parameters, best-fitting orbital solutions, and their uncertainties are presented in table 3, where K_b is the velocity semi-amplitude, P is the orbital period, $T_{\rm p}$ is the time of periastron passage, e is the eccentricity, ω is the argument of periastron, γ is the constant velocity, and $\dot{\gamma}$

Table 3. RV posterior distributions and priors.*

Parameter	Model A1	Model A2	Model B1	Model B2	Prior	Bound
K_b ($\mathrm{m\,s^{-1}}$)	$3.80^{+0.62}_{-0.58}$	$3.90^{+0.67}_{-0.61}$	$3.92^{+0.60}_{-0.58}$	$3.95^{+0.63}_{-0.59}$	Uniform	(0, 10)
P (d)	$10.76^{+0.01}_{-0.02}$	$10.77^{+0.01}_{-0.01}$	$10.77^{+0.01}_{-0.01}$	$10.77^{+0.01}_{-0.01}$	Uniform	(9, 12)
T_p (BJD −2450000)	$9370.22^{+1.38}_{-1.88}$	$9370.63^{+0.80}_{-0.84}$	$9370.24^{+0.64}_{-0.71}$	$9370.34^{+0.65}_{-0.60}$	Uniform	2459370 + (−6, +6)
e	0 (<0.70; 3σ)	$0.33^{+0.15}_{-0.17}$	$0.33^{+0.13}_{-0.15}$	$0.36^{+0.14}_{-0.16}$	Uniform	(0, 0.99)
ω (rad)		$-0.41^{+0.49}_{-0.50}$	$-0.65^{+0.39}_{-0.48}$	$-0.63^{+0.38}_{-0.44}$	Uniform	$(-\pi, +\pi)$
σ_{jitt} ($\mathrm{m\,s^{-1}}$)	$2.52^{+0.43}_{-0.41}$	$2.26^{+0.44}_{-0.42}$	$1.76^{+0.46}_{-0.48}$	$1.73^{+0.48}_{-0.49}$	Uniform	(0, 20)
γ ($\mathrm{m\,s^{-1}}$)	$-0.65^{+0.38}_{-0.38}$	$-0.28^{+0.38}_{-0.38}$	$-0.19^{+0.34}_{-0.34}$	$-0.08^{+0.35}_{-0.35}$	Uniform	(−20, +20)
γ_2 ($\mathrm{m\,s^{-1}}$)			$-7.68^{+1.26}_{-1.31}$	$-6.61^{+1.44}_{-1.36}$	Uniform	(−20, +20)
$\dot{\gamma}$ ($\mathrm{m\,s^{-1}\,yr^{-1}}$)		$2.03^{+0.62}_{-0.62}$		$0.89^{+0.62}_{-0.60}$	Uniform	(−10, +10)
$M_b \sin i$ ($M_\oplus$)	$3.99^{+0.60}_{-0.60}$	$3.96^{+0.59}_{-0.59}$	$4.00^{+0.53}_{-0.55}$	$3.97^{+0.54}_{-0.58}$		
a_b (au)	$0.05353^{+0.00047}_{-0.00051}$	$0.05361^{+0.00047}_{-0.00048}$	$0.05366^{+0.00056}_{-0.00049}$	$0.05356^{+0.00048}_{-0.00056}$		
rms ($\mathrm{m\,s^{-1}}$)		3.73	3.29	3.27		
Number of samples	16.0 M	13.8 M	24.0 M	20.5 M		
AIC	582.63†	573.79	553.63	553.44		
BIC	600.94†	602.56	582.39	584.82		
Description	Single planet	Model A1 + Linear trend	Single planet $+\gamma_2$	Model B1 + Linear trend		

*The e and ω were derived from $\sqrt{e}\sin(\omega)$ and $\sqrt{e}\cos(\omega)$.
†Assumed $e = 0$ as the best-fitting value.

is the constant RV acceleration (i.e., linear RV trend). The M_b, i, and a_b denote the mass of the planet, orbital inclination relative to line-of-sight, and its orbital semi-major axis, respectively.

A relatively large offset in RV measurements appears on 2021 August and September (see figure 8 in appendix 2). We wondered if these observations were influenced by a possible irregular and temporal offset in our RV measurements possibly caused by an instability of the instrument or a high-activity event such as flaring. Indeed, although the LFC's spectra have been stabilized for several years, the observing runs at 2021 August and September were immediately after the restoration from the irregular operation of the temperature stabilization room in which the LFC instrument are placed. Therefore, we compared two RV models: (A) one does not consider the RV offset in this period, and (B) the other assumes the RV offset as an additional systemic RV offset parameter in the RV model (γ_2).

We report the posterior median and 1σ credible region for each parameter in table 3. In our analysis, we compared four RV models in total:

- (A1) Single planet,
- (A2) model A1 + linear RV trend,
- (B1) single planet with RV offset for data in August and September of 2021 (i.e., γ_2), and
- (B2) model B1 + linear RV trend.

To perform model selection, we calculated the Akaike Information Criterion (AIC; Akaike 1974) and Bayesian Information Criterion (BIC; Schwarz 1978) for each of the four models, which are defined as

$$\mathrm{AIC} = 2k - 2\ln\mathcal{L} \tag{2}$$

and

$$\mathrm{BIC} = k\ln(N) - 2\ln\mathcal{L}, \tag{3}$$

where k is the number of parameters, N is the number of data points, and $\mathcal{L}$ is the maximum likelihood of the model.

Figure 3 shows the observed RVs and the orbital solutions from our MCMC analysis, and figure 4 shows a "corner" plot of the covariance between the parameters in our MCMC analysis. The BIC value is smaller for the model A1 than that of the model A2, while the AIC value is not. The ΔAIC and ΔBIC values are only slightly different from the values at which a model selection is statistically meaningful (Kass & Raftery 1995). We also found no clear statistical difference in the comparison between the B1 and B2, as indicated by the comparable BIC values. While Model A2 suggests a long-term trend, Model B2 did not, suggesting a degeneracy between the models of the linear RV trend and the temporal RV offset. Further investigation and additional data can resolve the degeneracy, but we

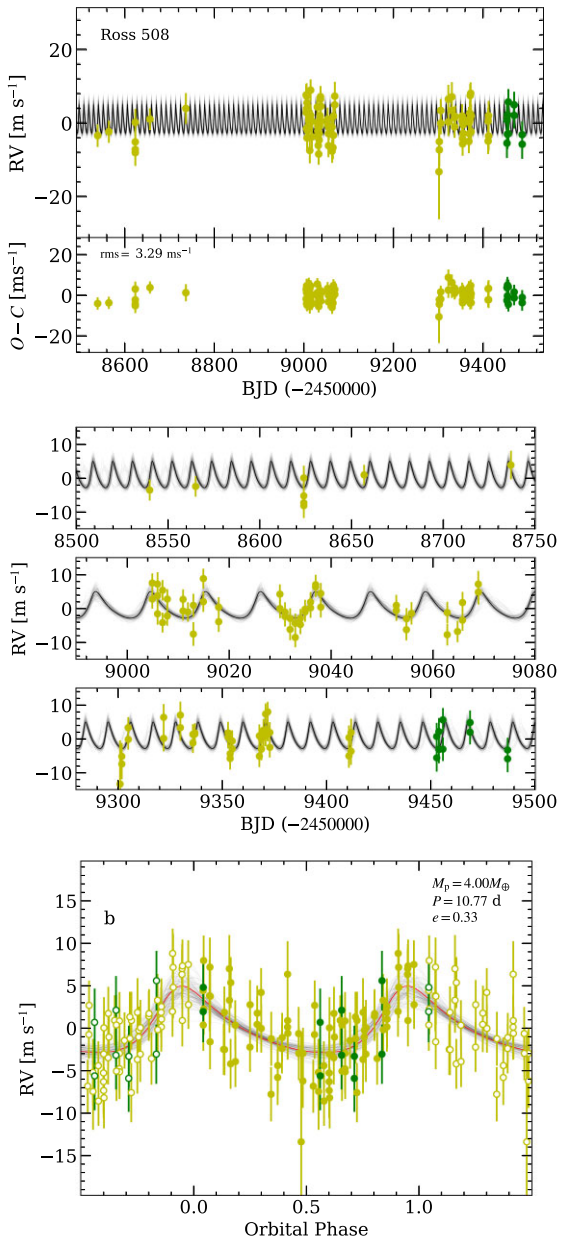

Fig. 3. Observed RVs and the best-fitting orbital solution based on the MCMC method of Model B1 (red line). Yellow circles with error bars represent the observed RVs and their uncertainties, respectively. Green circles and error bars show the same as yellow ones, but obtained in 2021 August and September. Gray lines represent 100 RV model curves randomly selected from the posterior. The error bars are the quadrature sum of the measurement uncertainties with the best-fitting value of the jitter parameter $\sigma_{\rm jitter}$. Top: Best fitting RV curve (top) and the residuals of the fit (bottom). Middle: Zoom in of each data segment. Bottom: Phase-folded RV variations. The red line represents the best-fitting RV model.

here conclude that there is no clear evidence to identify a long-term linear trend in our RV measurements.

The posterior eccentricity distribution of the model A1 monotonically decreases with a maximum at zero (figure 9 in appendix 2); we report only the 3σ upper limit for the eccentricity. Meanwhile, the posterior distributions of eccentricity for models A2, B1, and B2 have a maximum likelihood value around 0.3. However, a zero eccentricity is still likely as indicated by the eccentricity posterior in these three models. We therefore conclude that only an extremely high eccentricity, $e > 0.9$ (3σ), is unlikely. Furthermore, we adopt the model B1 (i.e., inclusion of no linear RV trend and a systematic RV offset) as our fiducial model based on the lowest AIC/BIC value among the four models.

3.4 Stellar activity

3.4.1 Photometric variability

While the RV data are well-fitted by a planetary companion, we now assess whether stellar activity could instead be responsible. To search for photometric modulation caused by stellar surface magnetic activity, we used the public archive data from the MEarth-North project (Berta et al. 2012) and the All-Sky Automated Survey for Supernovae (ASAS-SN; Shappee et al. 2014). We analyzed the MEarth data for Ross 508 from Data Release 10, and we selected data observed with the same telescope and RG715 filter bandpass at MEarth-North. We analyzed the *g*-band data from ASAS-SN. TESS will observe this target in Sector 51 (2022 April to May), which will allow us to characterize the stellar activity in more detail.

Newton et al. (2016) were not able to detect the rotation period of Ross 508. We independently analyzed the photometric data both from MEarth and ASAS-SN, and found no clear signals in the GLS periodogram that could be due to rotation or that match the observed RV signal (figure 2 for the periodogram on the MEarth light curves). In order to evaluate how small of a stellar-rotation modulation MEarth data can detect, we estimated the sensitivity of the MEarth data set to photometric modulation by creating 100 sinusoidal curves with periods of 10.8 d (the same as the detected planet's orbital period), with the same cadence as the actual MEarth data. We added white noise to each data point by sampling a Gaussian distribution with standard deviation equal to the individual photometric uncertainty of the corresponding data point, after scaling the median of the uncertainties to the standard deviation of all the data points in the MEarth light curve. We then applied a periodogram analysis to these mock data. We repeated the above analysis, varying the amplitudes of the sinusoidal curves. As per our definition, a periodic signal at 10.8 d can be detected if the FAP at that period is less than 1%. We found that 70% of the simulations yield a detection of the 10.8 d sinusoidal signal if its amplitude is larger than 0.4% of the stellar brightness in the MEarth photometric band. Similar results were obtained even if we shifted the

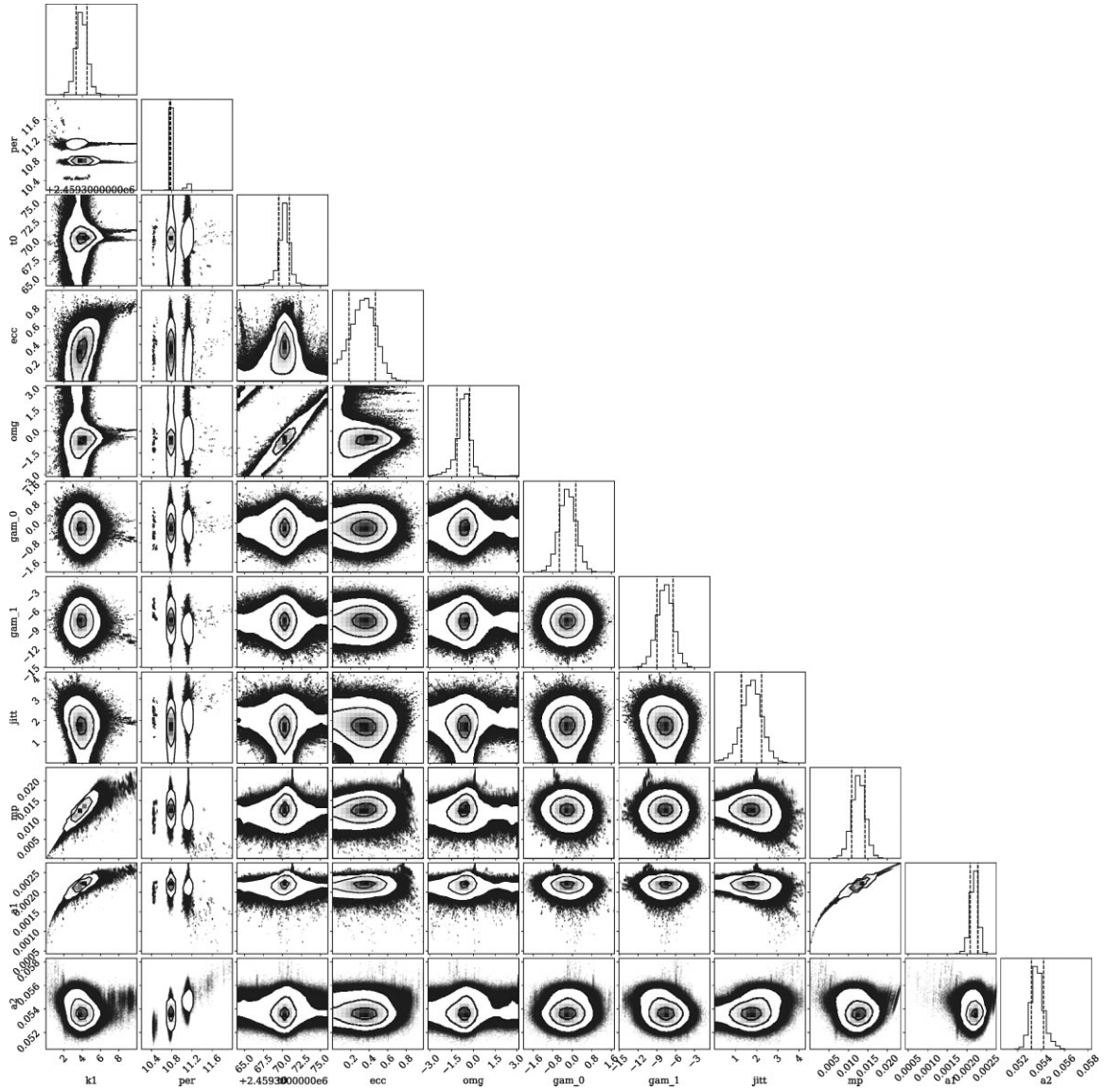

Fig. 4. Corner plot of the posterior distributions of Model B1.

phase of the sinusoidal signal or directly injected the sinusoidal curves into the MEarth light curves instead of creating mock data. However, even if there were a cool spot that produces a light-curve variation equal to or smaller than 0.4%, the corresponding RV semi-amplitude would be too small to account for our detected RV amplitude. Assuming the star's effective temperature, spot temperature, and rotation velocity ($v \sin i$) to be 3000 K, 2500 K, and 1 km s^{-1}, respectively, such a cool spot would induce an RV semi-amplitude of no more than 2 m s^{-1}. Here, the $v \sin i$ of 1 km s^{-1} is the maximum value estimated from the stellar radius of 0.213 $R_{\odot}$ (see table 1), assuming a rotation period equal to the detected RV period. Thus, a cool spot rotating with a period of 10.8 d and covering an area smaller than 0.4% of the stellar surface cannot reproduce our identified RV variation. Our light-curve analysis suggests that the 10.75 d signal is not caused by a cool spot on the stellar surface. We note that this analysis only applies if the phase of the photometric modulation is coherent over the ≈3 yr baseline of the IRD observations. However, the same criterion applies to the RV signal itself, which is indeed coherent in phase over this baseline.

3.4.2 Line profile variation

We next determine whether there is periodicity in the line profile at a period matching that of our recovered planet. We apply the least-squares deconvolution (LSD) method (Kochukhov et al. 2010) to derive mean line profiles. A list of lines is empirically built from an IP-deconvolved, telluric-free template spectrum. To minimize contamination, we use

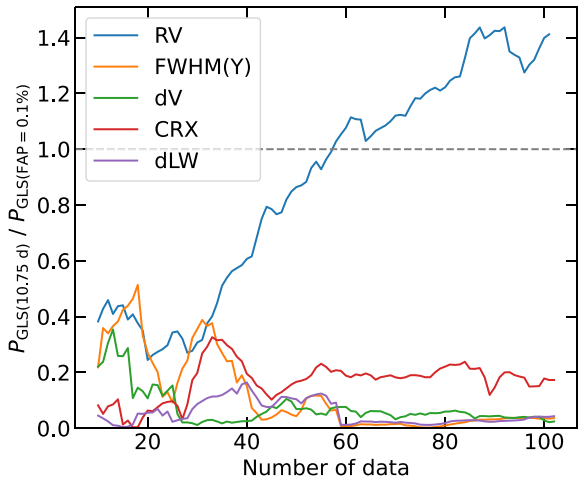

Fig. 5. Significance of the periodogram power for RVs and for all line-profile indexes as the number of data points increases. Significances are measured as fractions of the GLS power corresponding to FAP = 0.1%; the dashed gray horizontal line shows a value corresponding to FAP = 0.1% (i.e., 1.0).

spectra within 1000–1070 nm, which contain fewer telluric lines. The uncertainties of the LSD profiles are determined with formal uncertainties scaled by the standard deviations of the difference between each individual LSD and the mean profile. As indicators of line profile variation, we computed the full width at half maximum (FWHM; the line width) and BiGauss (dV; the line asymmetry) by fitting Gaussian functions (Santerne et al. 2015). We also computed the chromatic index (CRX; the wavelength dependence of RV) and the differential line width (dLW; the line width) (Zechmeister et al. 2018). To compute the dLW, we used a template spectrum convolved with the averaged IP instead of a coadded spectrum to avoid telluric-line contamination. To determine the CRX, the wavelength range is binned from 1000 to 1750 nm in 10 nm increments, and we use the weighted average of the RVs of the segments in each bin.

The GLS periodograms of all stellar activity indicators are shown in figure 2. None of the activity indicators exhibit any significant peaks at 10.75 d. Figure 5 shows the evolution of GLS power at 10.75 d for the RVs and activity indicators. While the power increases with the number of data points for the RVs, the power remains consistently low for the activity indicators, suggesting that the periodic RV variations are not induced by stellar activity (e.g., Mortier & Collier Cameron 2017).

4 Summary and discussion

In the previous section, we showed that the M4.5 dwarf Ross 508 has a significant RV periodicity at 10.75 d with possible aliases at 1.099 and 0.913 d. This periodicity has no counterpart in photometry or stellar activity indicators, but is well-fitted by a Keplerian orbit due to a new planet, Ross 508 b. Our newly discovered planet, Ross 508 b, has a minimum mass of 4.0 $M_\oplus$ and a semi-major axis of 0.05 au.

We explored four possible scenarios to explain the measured RV data. We examined models including a presence of RV offset to the data obtained in 2021 August and September, and a long-term RV trend, which might be caused by an unseen companion, because Ross 508 has a relatively high renormalized unit weight error (RUWE) of 1.48 in Gaia EDR3, suggesting that it is poorly fitted by a single star model. Of 19 comparison stars in EDR3 with parallaxes between 80 and 100 mas and $B_P - R_P$ colors within 0.3 mag of that of Ross 508, just three have RUWE values higher than 1.48.

While the differences between the four models are not large, we found that a $\sim$7 m s^{-1} RV offset and the absence of a long-term RV trend best explain the observed data. In this scenario, the peak of the posterior distribution of the eccentricity is around 0.3, but the distribution is wide all the way down to zero; hence it does not constrain the eccentricity well. As a reference, some previously known exoplanets around late-M dwarfs have eccentricities reported as upper limits, such as GJ 1061 b ($e < 0.31$), GJ 1061 d ($e < 0.53$; Dreizler et al. 2020) and Proxima Centauri b ($e < 0.35$; Anglada-Escudé et al. 2016; Brown 2017). Further RV measurements of Ross 508 will clarify whether the planet has a high eccentricity among the sample of known super-Earths around mid-to-late M stars ($T_{\rm eff} < 3200$ K, $M_p \sin i < 10 M_\oplus$), providing important clues about their origin.

As well as other super-Earths with orbital periods much shorter than the snow line around their host stars, Ross 508 b may have formed beyond the snow line ($\sim$0.16 au) and undergone inward Type I migration (Goldreich & Tremaine 1979; Ogihara & Ida 2009; Izidoro et al. 2017). Even if the eccentricity of a migrating planet is initially high, it can be damped by the force exerted on the planet by density waves (e.g., Tanaka & Ward 2004). Thus, the solution of a single-planet system with zero or low eccentricity is compatible with the Type I migration scenario. Alternatively, there remains the possibility that Ross 508 b is in a high-eccentricity orbit. In a multiple-planet system, migrated planets experience giant impacts or are trapped in a resonant chain (e.g., Ogihara & Ida 2009; Izidoro et al. 2017). Planetary eccentricities are excited by giant impacts. The eccentricity of a planet can be also excited by gravitational interactions between neighboring planets or secular perturbations from a (sub)stellar companion on a wider orbit. The confirmation of a long-term RV trend will help disentangle the formation history of the super-Earth Ross 508 b.

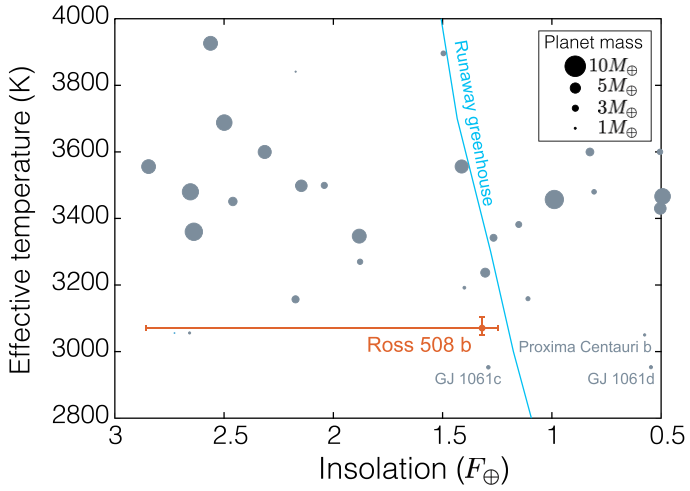

Fig. 6. Planets with masses below 10 $M_\oplus$ around stars with 2800 K $\leq T_{\rm eff} \leq$ 4000 K. Ross 508 b is located near the runaway greenhouse limit as the inner edge of a habitable zone for an Earth-sized aquaplanet around M dwarfs (Kopparapu et al. 2017). The error bar of Ross 508's insolation is based on the 3σ limit on its eccentricity.

The habitability of a planet primarily depends on the time-averaged stellar flux $\langle F \rangle$ that it receives over an entire orbit (Williams & Pollard 2002): $\langle F \rangle = F/\sqrt{1-e^2}$, where F is the stellar flux at the semi-major axis of a planet and e is the eccentricity of a planet. As shown in figure 6, the average insolation of Ross 508 b with an eccentricity ranging from 0 to 0.9 (which corresponds to a 3σ limit) is always higher than the runaway greenhouse limit for an Earth-sized aquaplanet around M dwarfs (Kopparapu et al. 2017). We note that the runaway greenhouse limit shown in figure 6 was estimated for an Earth-sized planet around a low-mass star with [Fe/H] = 0. The inner edge of the habitable zone may be farther from Ross 508 than what we calculated above because the low metallicity ([Fe/H] = −0.2) of Ross 508 yields a lower stellar luminosity (Kopparapu et al. 2016). Also, the habitability of super-Earths can be affected by climate and mantle dynamics, such as plate tectonics (e.g., Miyagoshi et al. 2018). The detailed characterization of Ross 508 helps understand the habitability of a super-Earth.

For compositional and atmospheric characterizations, it is advantageous if Ross 508 b transits the host star. The geometric transit probability (e.g., Kane & von Braun 2009) of Ross 508 b based on the best-fitting orbital parameters (Model B1) is estimated to be ≈1.6%; a small probability, but it is worth searching for their signals given the brightness of Ross 508 especially in the NIR. We visually inspected Ross 508's light curves using MEarth (subsection 3.4), and found no evidence for planetary transits of Ross 508 b. Fortunately, TESS is scheduled to observe Ross 508 in Sector 51 (2022 April to May), which would deliver Ross 508's light curve with a better precision. Provided that Ross 508 b has an internal composition similar to Earth, the expected depth of the transit is ≈ 0.3%, which is easily identified by the TESS photometry. Future atmospheric characterization of Ross 508 b makes it possible to explore the bulk composition of Ross 508 b and the formation mechanism of a massive terrestrial planet orbiting near the habitable zone.

Figure 7 places Ross 508 b in context with planetary systems around other nearby M-dwarfs; Ross 508 is one of the faintest, lowest-mass stars with an RV-detected planet. RV monitoring of such a faint, red star requires both a large telescope aperture and a high-precision spectrograph in the NIR. Future surveys with IRD and other high-precision NIR spectrographs will enable the discovery of planets around more stars like Ross 508, and will establish the diversity of their planetary systems. Exoplanet exploration will be advanced by the other late-M dwarf RV surveys using high-dispersion spectrographs, such as HPF, CARMENES, and SPIROU, as well as exoplanet surveys using the transit technique from space (e.g., TESS) and the ground (e.g., SPECULOOS; Delrez et al. 2018). Hence, the findings from various late-M dwarf observing campaigns in the 2020s will be combined to provide important clues to reveal the true nature of planetary systems around cool M dwarfs.

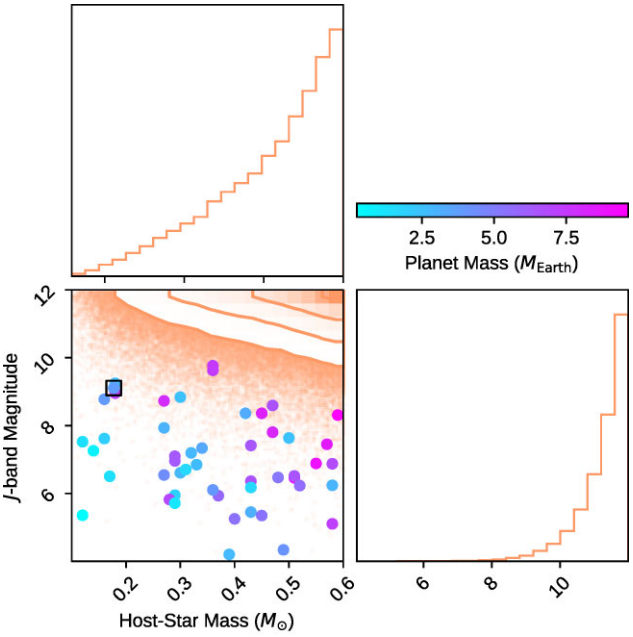

Fig. 7. Masses ($M_\odot$) and *J*-band magnitudes (mag) of *M*-type dwarfs that host RV-discovered planetary systems. The background contour shows the nearby *M*-type dwarfs taken from the TIC catalogue (Stassun et al. 2019). The filled circles are from the NASA exoplanet archive, with their *J*-band magnitudes from the 2MASS catalogue (Skrutskie et al. 2006). Note that we here plot only planetary systems hosting planets with masses lower than 10 $M_\oplus$. Ross 508, with parameters taken from table 1, is enclosed by a square box. The masses of the lowest-mass planets (which are also from the NASA Exoplanet Archive) in the systems are indicated by the color bar at the right-hand side of the upper panel. A low-mass planet recently discovered around Proxima Centauri (Faria et al. 2022) was included in the plots.

Acknowledgment

This research is based on data collected at the Subaru Telescope, which is operated by the National Astronomical Observatory of Japan. We are honored and grateful for the opportunity of observing the Universe from Maunakea, which has the cultural, historical, and natural significance in Hawaii. M.T. is supported by Japan Society for the Promotion of Science (JSPS) KAKENHI grant Nos. 18H05442, 15H02063, and 22000005. YH was partly supported by a Grant-in-Aid for Scientific Research on Innovative Areas (JSPS KAKENHI Grant Number 18H05439). This work is partly supported by JSPS KAKENHI Grant Numbers JP18H05439 and JP21K20388, Japan Science and Technology Agency (JST), Core Research for Evolutional Science and Technology (CREST) Grant Number JPMJCR1761, the Astrobiology Center of National Institutes of Natural Sciences (NINS) (Grant Number AB031010). This research has made use of the SIMBAD database, operated at CDS, Strasbourg, France (Wenger et al. 2000). This research made use of Astropy,[3] a community-developed core Python package for Astronomy (Astropy Collaboration 2013, 2018). This research has made use of the NASA Exoplanet Archive ⟨https://exoplanetarchive.ipac.caltech.edu⟩, which is operated by the California Institute of Technology, under contract with the National Aeronautics and Space Administration under the Exoplanet Exploration Program. This research has made use of data obtained from or tools provided by the portal exoplanet.eu of The Extrasolar Planets Encyclopaedia. The `corner` (Foreman-Mackey 2016) Python module has been helpful to create the figures in this paper.

[3] ⟨http://www.astropy.org⟩.

Appendix 1 Additional figures

Figures 8–13 show the best-fitting orbital solutions and the corner plots. Each pair of figures corresponds to models A1, A2, and B2, respectively.

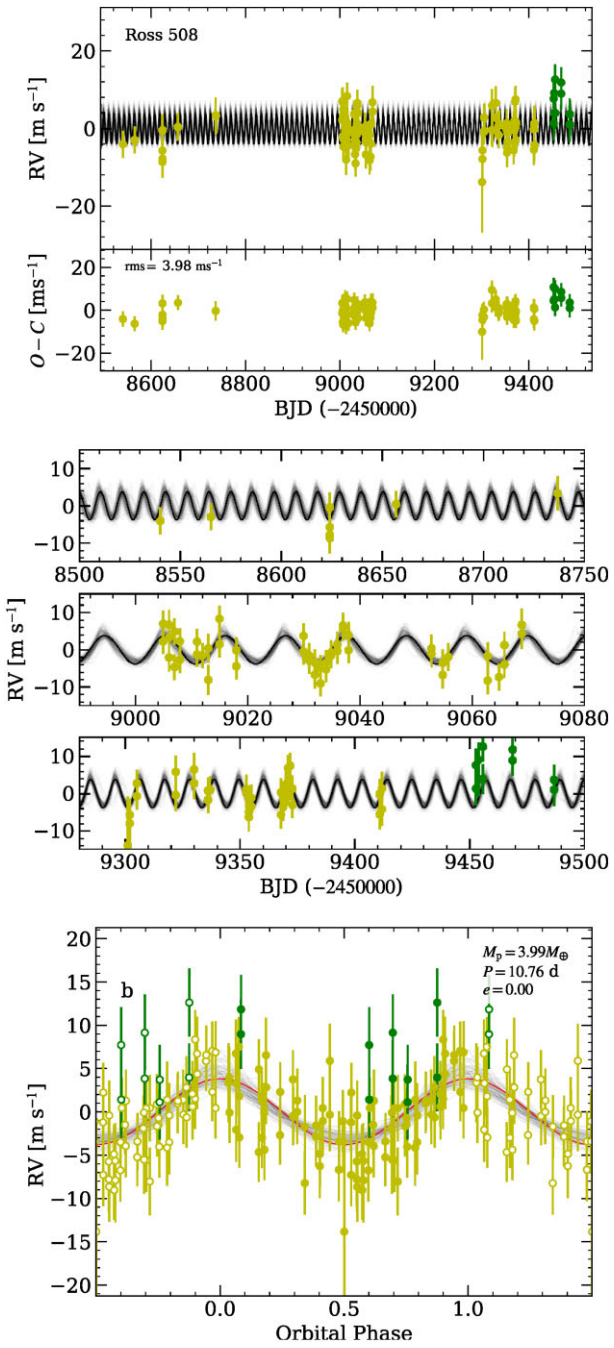

Fig. 8. Observed RVs and best-fitting RV model of Model A1. See caption to figure 3 for details.

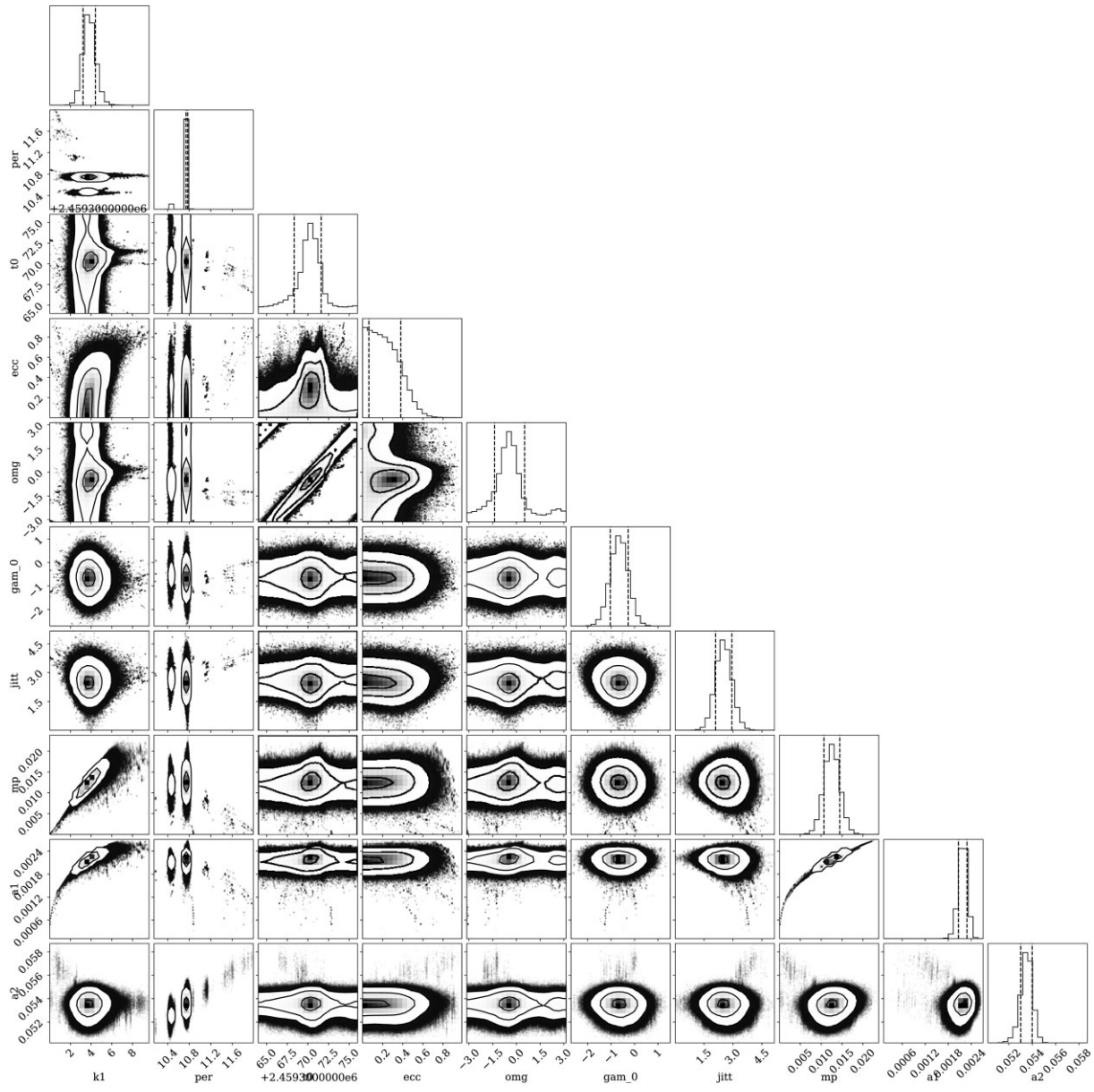

Fig. 9. Corner plot of Model A1.

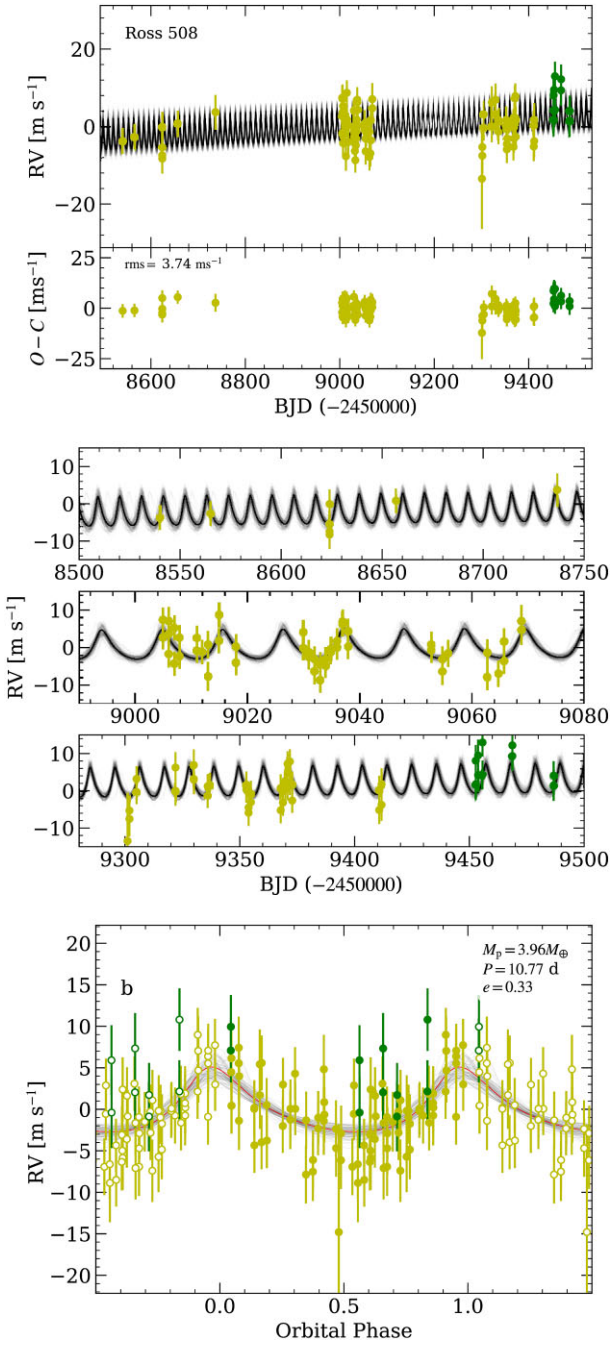

Fig. 10. Observed RVs and best-fitting RV model of Model A2. See caption to figure 3 for details.

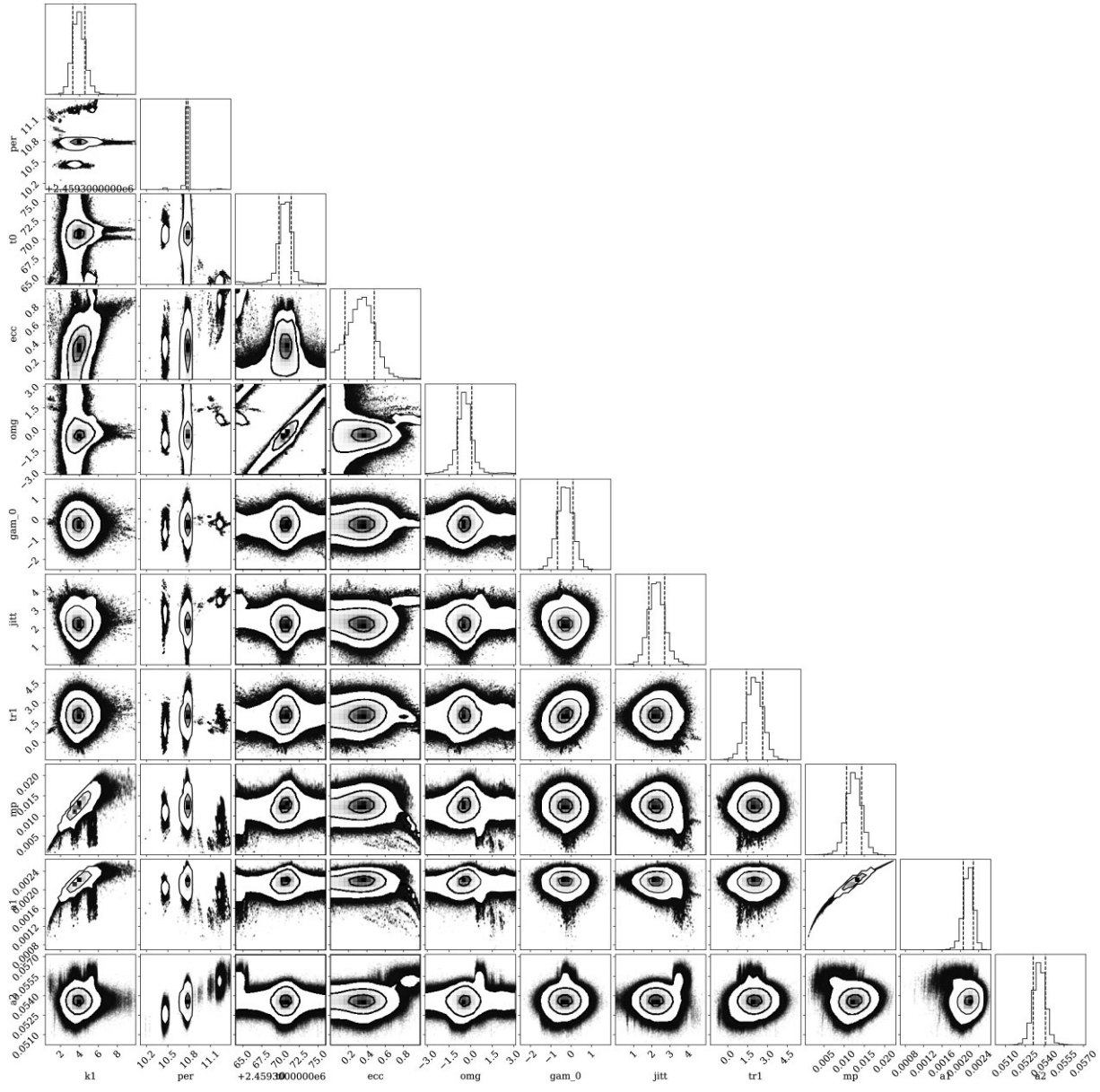

Fig. 11. Corner plot of Model A2.

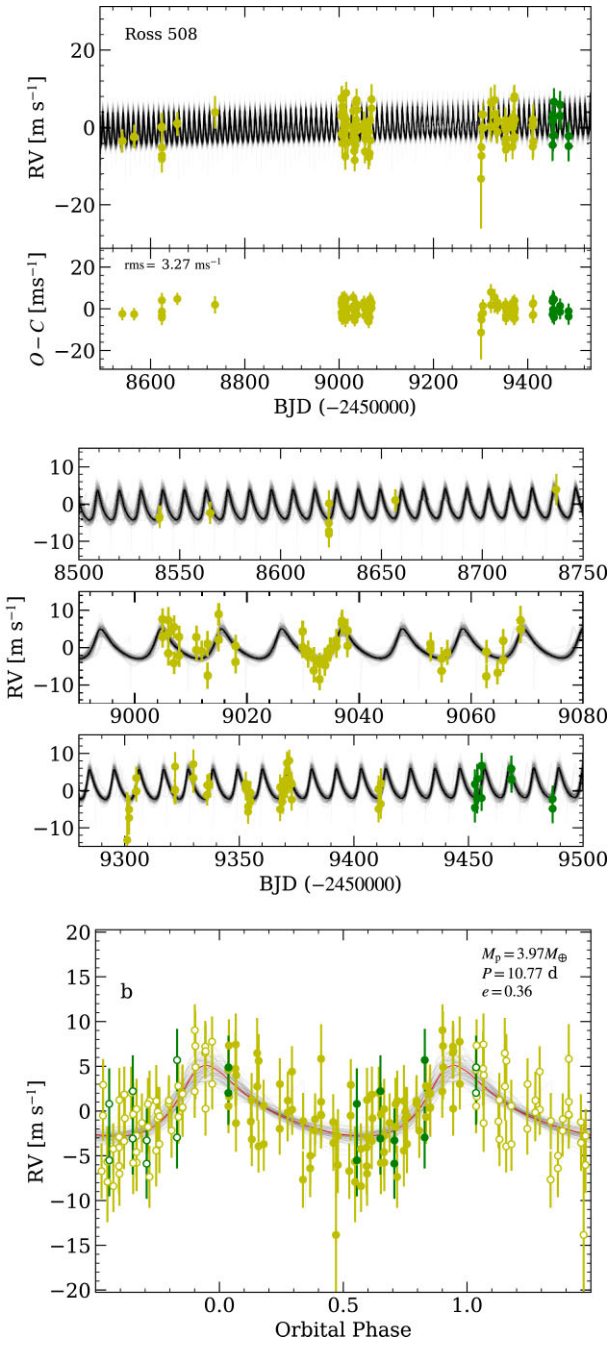

Fig. 12. Observed RVs and best-fitting RV model of Model B2. See caption to figure 3 for details.

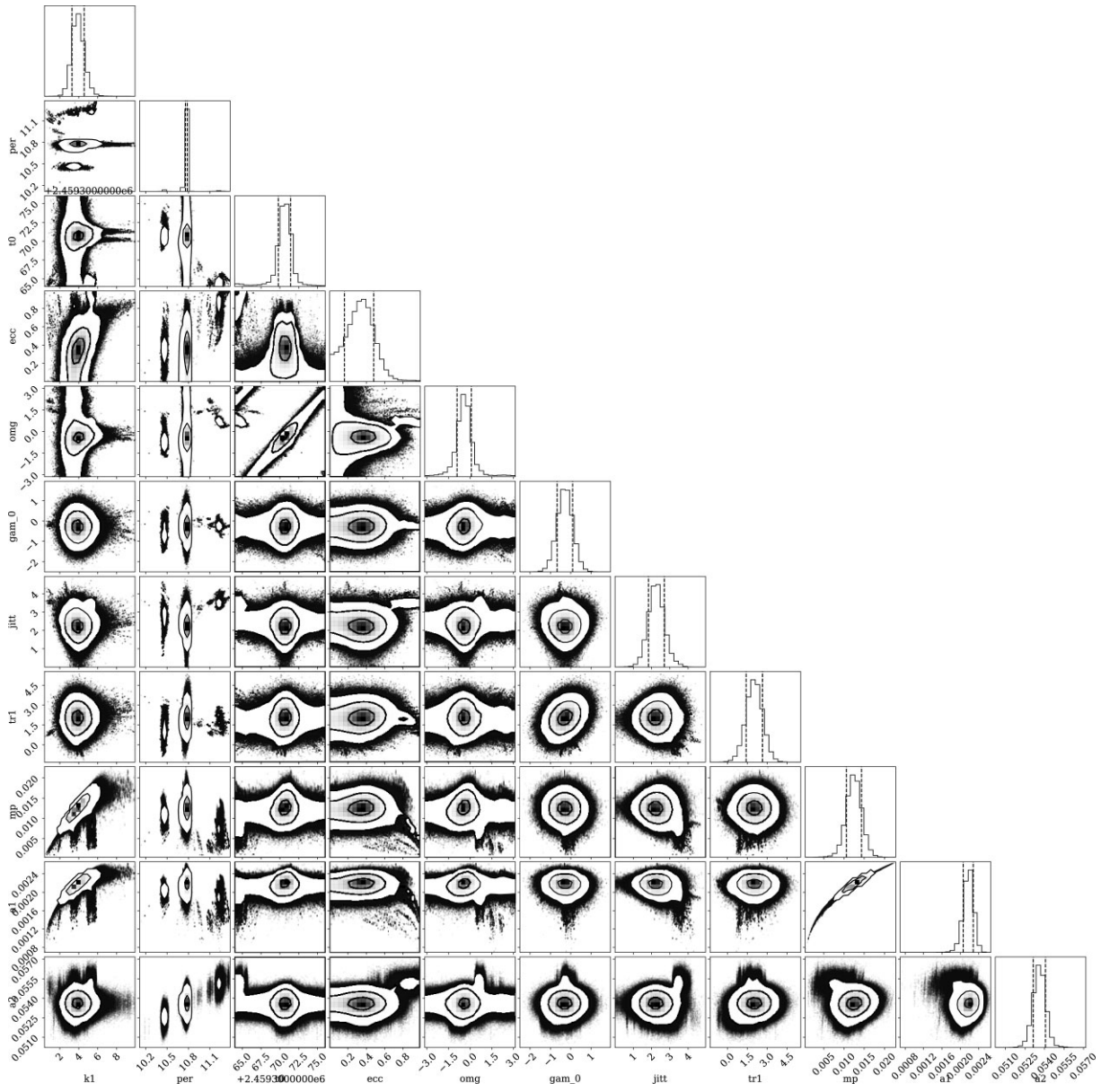

Fig. 13. Corner plot of Model B2.

References

Akaike, H. 1974, IEEE Trans. Automatic Control, 19, 716

Allard, F. 2014, in IAU Symp. 299, Exploring the Formation and Evolution of Planetary Systems, ed. M. Booth et al. (Cambridge: Cambridge University Press), 271

Anglada-Escudé, G., et al. 2016, Nature, 536, 437

Astropy Collaboration 2013, A&A, 558, A33

Astropy Collaboration 2018, AJ, 156, 123

Baglin, A., Auvergne, M., Barge, P., Deleuil, M., Catala, C., Michel, E., Weiss, W., & COROT Team, 2006, in Proc. The CoRoT Mission Pre-Launch Status - Stellar Seismology and Planet Finding, ed. M. Fridlund et al. (Noordwijk: ESA), 33

Bailer-Jones, C. A. L., Rybizki, J., Fouesneau, M., Demleitner, M., & Andrae, R. 2021, AJ, 161, 147

Baluev, R. V. 2008, MNRAS, 385, 1279

Baraffe, I., Chabrier, G., Barman, T. S., Allard, F., & Hauschildt, P. H. 2003, A&A, 402, 701

Berta, Z. K., Irwin, J., Charbonneau, D., Burke, C. J., & Falco, E. E. 2012, AJ, 144, 145

Borucki, W. J., et al. 2010, Science, 327, 977

Brandt, T. D., et al. 2013, ApJ, 764, 183

Brown, R. A. 2017, ApJ, 844, 100

Currie, T., et al. 2011, ApJ, 729, 128

Cutri, R. M., et al. 2021, VizieR Online Data Catalog, II/328

Delrez, L., et al. 2018, in Proc. SPIE, 10700, Ground-based and Airborne Telescopes VII, ed. H. K. Marshall & J. Spyromilio (Bellingham, WA: SPIE), 107001I

Dreizler, S., et al. 2020, MNRAS, 493, 536

Edwards, R. T., Hobbs, G. B., & Manchester, R. N. 2006, MNRAS, 372, 1549

Faria, J. P., et al. 2022, A&A, 658, A115
Foreman-Mackey, D. 2016, J. Open Source Software, 1, 24
Foreman-Mackey, D., Hogg, D. W., Lang, D., & Goodman, J. 2013, PASP, 125, 306
Gaia Collaboration 2021, A&A, 650, C3
Gillon, M., et al. 2017, Nature, 542, 456
Goldreich, P., & Tremaine, S. 1979, ApJ, 233, 857
Gregory, P. C. 2005, ApJ, 631, 1198
Hirano, T., et al. 2020, PASJ, 72, 93
Ishikawa, H. T., et al. 2022, AJ, 163, 72
Izidoro, A., Ogihara, M., Raymond, S. N., Morbidelli, A., Pierens, A., Bitsch, B., Cossou, C., & Hersant, F. 2017, MNRAS, 470, 1750
Kane, S. R., & von Braun, K. 2009, PASP, 121, 1096
Kashiwagi, K., Kurokawa, T., Okuyama, Y., Mori, T., Tanaka, Y., Yamamoto, Y., & Hirano, M. 2016, Opt. Exp., 24, 8120
Kass, R. E., & Raftery, A. E. 1995, J. Am. Statistical Assoc., 90, 773
Kochukhov, O., Makaganiuk, V., & Piskunov, N. 2010, A&A, 524, A5
Koizumi, Y., Kuzuhara, M., Omiya, M., Hirano, T., Wisniewski, J., Aoki, W., & Sato, B. 2021, PASJ, 73, 154
Kokubo, T., Mori, T., Kurokawa, T., Kashiwagi, K., Tanaka, Y., Kotani, T., Nishikawa, J., & Tamura, M. 2016, in Proc. SPIE, 9912, Advances in Optical and Mechanical Technologies for Telescopes and Instrumentation II, ed. R. Navarro & J. H. Burge (Bellingham, WA: SPIE), 599
Kopparapu, R. k., Wolf, E. T., Arney, G., Batalha, N. E., Haqq-Misra, J., Grimm, S. L., & Heng, K. 2017, ApJ, 845, 5
Kopparapu, R. k., Wolf, E. T., Haqq-Misra, J., Yang, J., Kasting, J. F., Meadows, V., Terrien, R., & Mahadevan, S. 2016, ApJ, 819, 84
Kotani, T., et al. 2018, in Proc. SPIE, 10702, Ground-based and Airborne Instrumentation for Astronomy VII, ed. C. J. Evans et al. (Bellingham, WA: SPIE), 1070211
Kuzuhara, M., et al. 2018, in Proc. SPIE, 10702, Ground-based and Airborne Instrumentation for Astronomy VII, ed. C. J. Evans et al. (Bellingham, WA: SPIE), 1070260
Lissauer, J. J., et al. 2011, Nature, 470, 53
Mahadevan, S., et al. 2014, in Proc. SPIE, 9147, Ground-based and Airborne Instrumentation for Astronomy V, ed. S. K. Ramsay et al. (Bellingham, WA: SPIE), 91471G
Mann, A. W., et al. 2019, ApJ, 871, 63
Mann, A. W., Feiden, G. A., Gaidos, E., Boyajian, T., & von Braun, K. 2015, ApJ, 804, 64
Mayor, M., & Queloz, D. 1995, Nature, 378, 355
Miyagoshi, T., Kameyama, M., & Ogawa, M. 2018, Earth, Planets, Space, 70, 200
Mortier, A., & Collier Cameron, A. 2017, A&A, 601, A110
Newton, E. R., Irwin, J., Charbonneau, D., Berta-Thompson, Z. K., Dittmann, J. A., & West, A. A. 2016, ApJ, 821, 93
Ogihara, M., & Ida, S. 2009, ApJ, 699, 824
Quirrenbach, A., et al. 2016, in Proc. SPIE, 9908, Ground-based and Airborne Instrumentation for Astronomy VI, ed. C. J. Evans et al. (Bellingham, WA: SPIE), 990812
Ricker, G. R., et al. 2015, J. Astron. Telesc., Instrum., Syst., 1, 014003
Santerne, A., et al. 2015, MNRAS, 451, 2337
Schneider, J., Dedieu, C., Le Sidaner, P., Savalle, R., & Zolotukhin, I. 2011, A&A, 532, A79
Schwarz, G. 1978, Ann. Statistics, 6, 461
Shappee, B. J., et al. 2014, ApJ, 788, 48
Skrutskie, M. F., et al. 2006, AJ, 131, 1163
Stassun, K. G., et al. 2019, AJ, 158, 138
Tamura, M., et al. 2012, in Proc. SPIE, 8446, Ground-based and Airborne Instrumentation for Astronomy IV, ed. I. S. McLean et al. (Bellingham, WA: SPIE), 84461T
Tanaka, H., & Ward, W. R. 2004, ApJ, 602, 388
Teng, H.-Y., et al. 2022, PASJ, 74, 92
Thibault, S., et al. 2012, in Proc. SPIE, 8446, Ground-based and Airborne Instrumentation for Astronomy IV, ed. I. S. McLean et al. (Bellingham, WA: SPIE), 844630
Vanderburg, A., et al. 2020, Nature, 585, 363
Wenger, M., et al. 2000, A&AS, 143, 9
Williams, D. M., & Pollard, D. 2002, Int. J. Astrobiology, 1, 61
Zechmeister, M., et al. 2018, A&A, 609, A12
Zechmeister, M., et al. 2019, A&A, 627, A49
Zechmeister, M., & Kürster, M. 2009, A&A, 496, 577